A 9 myr cycle in Cenozoicδ13C record and long-term orbital eccentricity modulation: Is there a link?

Slah Boulila, Bruno Galbrun, Jacques Laskar, Heiko Pälike

Accepted Manuscript (Nov. 18, 2011), Earth and Planetary Science Letters
v. 317–318, p. 273–281, 2012, doi:10.1016/j.epsl.2011.11.017.

A ~9 myr cycle in Cenozoic $\delta^{13}C$ record and long-term orbital eccentricity modulation: Is there a link?

Slah Boulila [a,b,*], Bruno Galbrun [a], Jacques Laskar [b], and Heiko Pälike [c]

[a] Université Paris VI, CNRS - UMR 7193 ISTeP 'Institut des Sciences de la Terre-Paris', case 117, 4, place Jussieu, 75252 Paris cedex 05, France

[b] ASD, IMCCE-CNRS UMR8028, Observatoire de Paris, UPMC, 77 avenue Denfert-Rochereau, 75014 Paris, France

[c] National Oceanography Centre, Southampton, School of Ocean and Earth Science, European Way, Southampton SO14 3ZH, UK

* Corresponding author. Tel.: +33 144274163; Fax: +33 144273831

Email addresses: slah.boulila@upmc.fr (S. Boulila), bruno.galbrun@upmc.fr (B. Galbrun), laskar@imcce.fr (J. Laskar), H.Palike@soton.ac.uk (H. Pälike).

Abstract

The ~65-myr-long Cenozoic carbon isotope record ($\delta^{13}C$) of Zachos et al. (2001, 2008) documents a strong long-term cycle with a mean pseudoperiodicity close to ~9 myr.

This cyclicity modulates the ~2.4 myr eccentricity cycle amplitude, hinting at a possible link between long-term astronomical and geological variations. Some phase shifts between ~9-myr $\delta^{13}C$ and astronomical cycles suggest that additional processes (e.g., tectonics) contribute to these long-term carbon-cycle variations.

The strong response of $\delta^{13}C$ to long-term eccentricity periods (~9 myr, ~2.4 myr, ~400 kyr) supports the hypothesis that the long time-residence of carbon in the oceans amplifies lower frequency or dampens higher frequency orbital variations. Additionally, the strong expression of low-amplitude ~9 myr eccentricity cycle in the $\delta^{13}C$ record could be explained by energy-transfer process from higher to lower frequency cycles, and all eccentricity components modulate the carrier climatic precession cycles.

Finally, the Paleocene-Eocene Thermal Maximum (PETM, 55.9 Ma) event, which corresponds to a pronounced $\delta^{13}C$ negative excursion, is situated within a strong decrease in the most prominent ~9 myr $\delta^{13}C$ cycle, hinting at a link between accelerated rates in $\delta^{13}C$ variations and the PETM. This specific ~9 myr $\delta^{13}C$ cycle seems to be amplified by non-orbital mechanisms in atmosphere-continent-ocean system, such as previously suggested methane release from gas hydrate and volcanism.

Keywords: Cenozoic deep-sea $\delta^{13}C$ records, multi-millionyear cyclicity, ~9 myr cyclicity, astronomical driving force, eccentricity.

1. Introduction

54 It has been widely demonstrated that Earth's orbital parameters (climatic precession,
55 obliquity, eccentricity) control paleoclimate changes induced by variations in solar radiation
56 intensity received by our planet (Hays et al., 1976; Imbrie et al., 1984). Research has
57 documented the Earth's orbital parameters in the geologic record over broad time scales,
58 from millennial to million year time scales. Today, there is a broad consensus that insolation
59 forcing from the Earth's orbital parameters is a major external driver of changes in
60 atmospheric, continental, and oceanic conditions across all latitudes. Accordingly, recent
61 research has now turned to explain extreme short-lived climate events (e.g., Lourens et al.,
62 2005), ice-sheet formation and carbon reservoir cycling (e.g., Pälike et al., 2006a), biotic
63 extinctions (van Dam et al., 2006), and other poorly understood phenomena. Reciprocally,
64 geophysical processes, such as a post-glacial rebound (Laskar et al., 1993; Mitrovica et al.,
65 1997) and mantle convection (Forte & Mitrovica, 1997), could have influenced secular
66 variations in the dynamic ellipticity of the Earth, which consequently influence the
67 astronomical precession constant value (e.g., Berger et al., 1992).

68 In this study, we focus on very long-term periodic variations in the carbon isotope
69 record ($\delta^{13}C$) of Cenozoic deep-sea sediments by which we suggest a possible link with long-
70 term astronomical modulation cycle. Numerous Cenozoic and Mesozoic studies have
71 interpreted these long-term carbon cycle variations as trends, most of them suggesting a
72 tectonic origin (e.g., Zachos et al., 2001; Leckie et al., 2002; Li et al., 2009). Through a
73 comparison between long-term $\delta^{13}C$ cycle and orbital eccentricity modulation cycle, we
74 suggest another alternative, i.e., orbital driving force.

75 Additionally, our results concur with and build on previous studies pointing to the long
76 residence-time of carbon in oceans amplified by longer orbital periods (Pälike et al., 2006a).
77 At the same time, we do not rule out possible interactions between tectono-oceanic and
78 climatic variations (e.g., Raymo and Ruddiman, 1992; Lagabrielle et al., 2009) in carbon
79 recycling, triggered or retroacted by the astronomical driving force.

2. Cenozoic carbon isotope record ($\delta^{13}C$)

Building on ocean drilling during the last three decades, ~65-myr-long Cenozoic carbon and oxygen records ($\delta^{13}C$ and $\delta^{18}O$) were compiled from benthic foraminifera isotope data from more than 40 deep-sea cores of the Deep Sea Drilling Project (DSDP) and Ocean Drilling Program (ODP) (Zachos et al., 2001, 2008, Fig. S1, and Cramer et al., 2009). Today, these long records serve as a basic reference for numerous Cenozoic paleoclimate studies that address rhythms, trends and events in Earth's changing climate (Zachos et al., 2001). The compiled records of Zachos et al.'s (2008) compilation exhibit variable resolution, which is comprised between less than ~1 kyr and ~8 kyr for the last ~34 Ma, and could reach 40 kyr for the last 35 to 65 Ma interval (Zachos et al., 2008). This resolution of the stacked data is however sufficient for time-series analysis of low-frequency (multi-millionyear) variations. In this study, we examine the behavior of long-period cycles in the $\delta^{13}C$ record (Fig. 1), and in particular, we suggest a possible link with long-term eccentricity cycling throughout the Cenozoic (Section 3).

The ~65-myr-long Cenozoic carbon record shows evidence of ~9-myr cycles that we denote as Cb1 to Cb8 (Fig. 1). Zachos et al.'s (2001) studies were focused on oxygen isotope evolution to interpret temperature and glacial trends and short-lived events such as the Paleocene-Eocene Thermal Maximum (PETM), Oi-1, Mi-1 glaciation events, etc. The Oi-1 and Mi-1 events delimit the Cb4 cycle, which roughly spans the Oligocene Epoch. This cycle was studied in detail by Pälike et al. (2006a) at a ~4-kyr sampling resolution (Fig. 2a), who demonstrated the strong expression of the ~400-kyr cycles in the carbon isotope signal. Filtering and modulation analysis studies were focused mainly on the ~100-kyr eccentricity and 41-kyr obliquity bands to recover the important ~1.2 and ~2.4-myr astronomical

105 modulations. Modulation behavior of the lower frequency ~400-kyr and ~2.4-myr eccentricity
106 cycles (Section 3.2) were not examined.
107 In fact, because the Oligocene interval is only 11.9-myr long (from 22 to 33.9 Ma),
108 Pälike et al. (2006a) did not consider Cb4 to be a true cycle (Section 3). Instead, they
109 subdivided the interval into 4 phases, which they interpreted as long-term trends, through
110 comparison with the oxygen isotope record (see their Figure 1). Here, we show that this
111 cycle, Cb4, contains four ~2.4-myr cycles easily correlatable to their analogs in astronomical
112 solutions (Laskar et al., 2004, and Laskar et al., 2011a). The ~2.4-myr term acts to modulate
113 the ~400-kyr cycles, while the 'Cb4' modulates the 2.4-myr cycles (Figs. 1 and 2a, Section
114 3.2).
115
116 **3. Methods and results**
117
118 **3.1. Spectral analysis**
119
120 **3.1.1. Spectral analysis of $\delta^{13}C$ data**
121
122 Spectral analysis of the raw $\delta^{13}C$ record of Zachos et al.'s (2008) compilation shows
123 two dominant peaks centered on periods of 27 and 8.4 myr (Fig. 3a). Similar results are
124 obtained when we consider the same interval (i.e., Cenozoic) in Cramer et al.'s (2009) $\delta^{13}C$
125 compilation (Fig. 3b). The 8.4 myr cyclicity is prominent in the $\delta^{13}C$ records and represent the
126 cycles denoted Cb1 to Cb8 (Fig. 1). Its pseudo-period could vary from ~7.5 myr (Cb2) to ~11
127 myr (Cb3). However, the 27 myr peak is not evident in $\delta^{13}C$ time series, but it may
128 correspond to the two cycles delimited by the minima of Cb1, Cb4 and Cb7 (Figs. S1 and
129 S2). These very long-term $\delta^{13}C$ oscillations have a significant effect on spectral results. When
130 we subtract them, other peaks at higher frequency band are strengthened, but still with low

power because of the high-power ~9 myr peak (Fig. S2). To highlight low- and high-frequency bands, we display the raw $\delta^{13}C$ spectrum, associated with the robust noise, on a logarithmic scale (Figs. 3c,d). Zachos et al.'s (2008) compilation (Fig. 3c) shows several spectral peaks around the 400 kyr band, but none of them matches the astronomically predicted and well defined 405 kyr eccentricity term; one peak centered on the period of 1.2 myr, likely related to long-term obliquity modulation cycle; and two other peaks at 1.9 and 2.5 myr periods, may represent the 2.4 myr orbital eccentricity term. Cramer et al.'s (2009) compilation (Fig. 3d) shows also several peaks around the 400 kyr band, only one peak (404 kyr, see also Fig. S2) may correspond to the 405 kyr eccentricity period. This mismatch between $\delta^{13}C$ and astronomical periodicities may be due to the sampling rates in these stacked $\delta^{13}C$ data (see Section 3.2). Differences in spectral analysis results between the two $\delta^{13}C$ compilations (i.e., Zachos et al., 2008; Cramer et al., 2009) concur with this hypothesis of the sampling-rate effect. Nevertheless, the multi-myr $\delta^{13}C$ cycles are robust and persistent in both compilations (Figs. 3a,b). Particularly, the ~9 myr cycles are well detected by lowpass and bandpass filtering of the two $\delta^{13}C$ time series (Fig. 1). The 405 kyr and 2.4 myr $\delta^{13}C$ cyclicities are documented with confidence in the single ODP site 1218 (Fig. 2a, Pälike et al., 2006a), which respectively reflect 'g2-g5' and 'g4-g3' eccentricity terms (where g2, g3, g4, and g5 are respectively related to the precession of the perihelions of Venus, the Earth, Mars, and Jupiter, Fig. 4). However, neither 8.4 nor 27-myr cycles is evident in the Earth's orbital variations (e.g., Laskar et al., 2004). To determine if these long-term cycles have an astronomical origin, we tested their presence in two astronomical models, La2004 and the most recent and constrained La2010d (Laskar et al., 2004; Laskar et al., 2011a).

3.1.2. Spectral analysis of the orbital eccentricity variations

156 The objective of this section is to test if there are small (low amplitudes) low-
157 frequency (periods longer than ~2.4 myr) cyclicities in the raw eccentricity time series. Thus,
158 we applied spectral analysis (Figs. 4a,b) to the La2004 and La2010d orbital eccentricity for
159 the last 67 Ma (time interval equivalent to that in $\delta^{13}C$ records).
160
161 The La2004 model was demonstrated as precise for the last 40 Ma (Laskar et al.,
162 2004). The La2010d is the most constrained version of the La2010 astronomical model that
163 extends the precision to the last 50 Ma (Laskar et al., 2011a,b). The main difference between
164 La2004 and La2010 models is that the La2004 initial conditions are ajusted to the JPL
165 numerical ephemeris DE406 (Standish, 1998) over –5000 yr to +1000 yr from the present
166 date, while La2010 is fitted to the most precise planetary ephemeris INPOP06 and INPOP08
167 (Fienga et al., 2008, 2009). In particular, La2010d version is adjusted to the INPOP06 over
168 the last 1 Ma that includes the five major asteroids, Ceres, Vesta, Pallas, Iris, and Bamberga.
169 La2010a, La2010b and La2010c are fitted to the INPOP08 over only 580 kyr for La2010a
170 and La2010b, and over 1 myr for La2010c. However, the latter does not include the five
171 major asteroids, Ceres, Vesta, Pallas, Iris, and Bamberga. Certain orbits of these asteroids
172 underwent a strong chaotic behavior, and consequently their motion will be unpredictable
173 over 400 kyr, which in turn influences the Earth's orbital eccentricity calculation (for detail see
174 Laskar et al., 2010b). Thus, the La2010d version is considered as the most constrained
175 version in the La2010 model (Laskar et al., 2010b).
176
177 Frequency decomposition in harmonic analysis of both La2004 and La2010d raw
178 eccentricity are very similar (Figs. 4a,b). However, the relative amplitudes of spectral peaks
179 are slight different; this difference is linked to the parameters used in each astronomical
180 model (detailed in Laskar et al., 2011a). At the low frequencies, amplitude spectrum (Fig. 4b)
181 shows peaks around the 400-kyr band, i.e., (g2 – g5) and (g2 – g5) ± (g4 – g3) terms

182 composed of the three periods 405 kyr for (g2 – g5), 489 kyr for (g2 – g5) – (g4 – g3), and
183 345 kyr for (g2 – g5) + (g4 – g3) (Fig. 4, see Laskar et al., 2004, their table 6). The
184 interference of the two coupled periods (405 with 345 kyr, and 405 with 489 kyr) induces the
185 long ~2.4 myr eccentricity term, i.e., (g4 – g3), which is represented by a significant peak
186 (Fig. 4b, see Section 3.2.1). Two other main peaks at 670 and 959 kyr correspond
187 respectively to (g2 – g1) and (g1 – g5) terms. Finally, a weak peak centered on the period of
188 ~4.5 myr corresponds to another eccentricity term discussed in Section 3.2.1.
189
190 Lowpass filtering does not show significant low-frequency (longer than ~4.5 myr)
191 variations given that, if present, they are with very low energy as illustrated in the amplitude
192 spectra (Fig. 4b). Nevertheless, low-amplitude astronomical variations could have significant
193 influence on Earth's climate change. As an example, though the direct effect of eccentricity
194 forcing on insolation is relatively low, the strong imprint of the main eccentricity cycles (the
195 average 97, 128 kyr, and the strong single 405 kyr; Fig. 4a) in paleoclimatic variations could
196 be indirect, i.e., via energy transfer from the carrier climatic precession into the modulator
197 eccentricity. Same behavior could manifest in the very low-frequency eccentricity terms
198 (Section 3.2.1), where energy could be transferred from higher to lower frequency terms via
199 amplitude/frequency modulation, and all eccentrcity terms modulate, in turn, the precession
200 index cycles. The most compelling example is that the ~2.4 myr eccentricity term (g4 – g3)
201 with relatively low amplitude (e.g., Laskar et al., 2004) is well recognized in geological
202 records (Olsen and Kent, 1999; Hilgen et al., 2003; van Dam et al., 2006; Mitchell et al.,
203 2008; Abels et al., 2010; and many others), while it could act as a modulator of higher
204 frequency eccentricity terms, either at the 100 k.y. or at the 400 k.y. cycle bands (e.g., 405
205 with 489 kyr, and 405 with 345 kyr, Fig. 4b, Section 3.2.1). Another striking example
206 concerns the Earth's obliquity variations. In particular, the ~1.2 myr obliquity cycle is strongly
207 documented in Cenozoic icehouse strata (e.g., Wade and Pälike, 2004; Pälike et al., 2006a),
208 although it only acts as a modulator of the higher frequency obliquity cycles (i.e., p + s3 ≈ 41

kyr and p + s4 ≈ 39.6 kyr). Thus, these examples indicate that the presence of a long-period astronomical cycle with low amplitude, but with a strong imprint in a paleoclimatic record is possible via amplitude/frequency modulation of the higher frequency cycles, and the consequent energy-transfer process. Therefore, we tested possible very long-period eccentricity cycles via amplitude modulation (AM) technique.

We performed AM analysis on both the raw $\delta^{13}C$ data and the orbital eccentricity, in order to seek possible analogs. We focused on the ~400-kyr and ~2.4-myr cycles because of their strength in the $\delta^{13}C$ record (Fig. 2a), even if they seem to be biaised by the stacked sampling rates (Figs. 3c,d), and low resolution of the early Cenozoic $\delta^{13}C$ data (Fig. S3).

3.2. Amplitude modulation (AM) analysis

First, we bandpass-filtered the orbital eccentricity ~100-kyr, ~400-kyr and ~2.4-myr variations, and performed Hilbert transforms (e.g., p. 435 in Hinnov, 2000) on the filtered series (Fig. 1). Then, we applied the same procedure to the $\delta^{13}C$ record, but only at the longer periods, i.e. ~400-kyr and ~2.4-myr (Fig. S3), because the $\delta^{13}C$ data resolution is too low to adequately recover ~100-kyr scale behavior through the past 65 Ma, and the stacked sampling rates have a significant effect on higher frequency band (Figs. 3c,d; Section 3.1). Finally, we applied spectral analysis on the amplitude modulation (AM) envelopes (Figs. 5 and 6).

3.2.1. AM of the orbital eccentricity

Time-series analysis of astronomical AM envelopes shows significant long-term modulations in the eccentricity bands. The AM envelope of the short eccentricity (~100-kyr) shows strong 0.405- and 2.4-myr modulations (Fig. 5a), whereas those of the ~400-kyr

235 eccentricity shows strong ~2.4-myr and lesser ~4.5-myr modulations (Figs. 5b and S4). The
236 AM envelope of the ~2.4-myr orbital eccentricity band shows ~9-myr and ~26-myr cyclicity
237 (Figs. 5c,d). The latter is not obvious in the AM time series. However, the former is well
238 detected in AM time series, and shows some correlation with the $\delta^{13}C$ record (Section 4).
239 Thus, the ~4.5- and ~9-myr cyclicities are present in the orbital eccentricity modulations. The
240 ~2.4-myr component could derive from the interference of the two coupled close frequencies
241 in the 400 kyr band (Fig. 4b). In particular, the interferences of 405 kyr (g2 – g5) with 345 kyr
242 ((g2 – g5) + (g4 – g3)), and 405 kyr (g2 – g5) with 489 kyr ((g2 – g5) – (g4 – g3)) induce both
243 the 2.4 myr term (g4 – g3) (see Fig. 4b). The astronomical origin of the ~4.5-myr cycles was
244 discussed in Laskar (1990) as deriving from the resonant argument $\theta = 2(g_4 - g_3) - (s_4 - s_3)$,
245 where g_3, g_4 are related to the precession of the perihelions of the Earth and Mars, s_3, s_4 are
246 related to the precession of the nodes of the same planets. The ~4.5-myr cyclicity is present
247 in the orbital eccentricity solution (Fig. S5). However, the ~9-myr was not previously
248 explicited in the astronomical models.
249
250 **3.2.2. AM of the $\delta^{13}C$ variations**
251
252 Then, we performed ~400-kyr and ~2.4-myr AM analysis on the $\delta^{13}C$ records of
253 Zachos et al.'s (2008) and Cramer et al.'s (2009) compilations (Figs. 6 and S3). The
254 spectrum of ~400-kyr AM of Zachos et al.'s compilation (Fig. 6a) shows a strong significant
255 peak centered on 5 myr, and two other weaker but significant peaks of periods 3.8 and 1.9
256 myr. The 5- and 3.8-myr peaks may represent the average of the ~4.5-myr periodicity
257 (discussed previously). The 1.9 myr peak could represent a distorted ~2.4-myr eccentricity
258 modulation term (see below). The spectrum of ~400-kyr AM of Cramer et al.'s compilation
259 (Fig. 6b) indicates two strong significant peaks centered on 2.4 and 16 myr. The former

corresponds likely to 'g4-g3' eccentricity term (Fig. 5b). However, the latter is not evident neither in the astronomical variations nor in the $\delta^{13}C$ time series.

The spectrum of ~2.4-myr AM of Zachos et al.'s compilation (Fig. 6c) shows mainly four significant peaks (above 99% CL) centered on the periods of 6.3, 8.1, 12, and 32 myr. The three first ones, with an average of 8.8 myr, may represent the ~9 myr astronomical variations. The latter again is not evident in the $\delta^{13}C$ time series. The spectrum of ~2.4-myr AM of Cramer et al.'s compilation (Fig. 6d) highlights three significant peaks centered on the periods of 7.4, 10.2, and 27.5 myr. The former two, with an average of 8.8 myr, most likely represent the ~9 myr astronomical variations. The latter may represent the peak seen in the raw $\delta^{13}C$ spectrum (i.e., 29 myr, Fig. 3b). Therefore, AM results suggest that the ~9-myr cyclicity modulates the ~2.4-myr and not the ~400-kyr cycles as has been demonstrated in the astronomical models. Additionally, AM results of the 2.4 myr band is more consistent than those of the 400 kyr band. This again suggests the more effect of sampling rates on higher frequency cycles. In sum, despite of the Cramer et al.'s (2009) compilation show some $\delta^{13}C$ frequencies, in the ~2.4-myr AM, consistent with astronomical frequencies, the large differences of AM outputs (Figs. 6 and S3) between the two $\delta^{13}C$ versions (Zachos et al., 2008; Cramer et al., 2009) preclude any positive conclusion regarding AM results. The stacked sampling rates could be the most important factor that affects the documentation of higher frequency cycles, and hence AM use, given that both $\delta^{13}C$ compilations are rescaled to the same timescale (GTS2004, Gradstein et al., 2004). Nevertheless, the ~9 myr cycles are prominent and robust in both $\delta^{13}C$ compilations.

4. $\delta^{13}C$ variations and orbital eccentricity correlation

285 The 9-myr eccentricity cycles correlate well with the raw $\delta^{13}C$ (Fig. 1) because of the
286 higher sensitivity of global carbon-cycle to eccentricity forcing (e.g., Cramer et al., 2003;
287 Pälike et al., 2006a; Abels et al., 2010). A clear negative correlation between eccentricity and
288 $\delta^{13}C$ cycles was observed from ~8 to ~60 Ma. Maxima of $\delta^{13}C$ correspond to minima of ~9
289 myr eccentricity cycles. Similar negative correlation was also demonstrated at the higher
290 frequency eccentricity cycles (~2.4-myr, ~400-kyr, and ~100-kyr, Cramer et al., 2003; Pälike
291 et al., 2006a, and many others). Cb1 to Cb8 $\delta^{13}C$ cycles correlate well with the ~9 myr
292 astronomical cycles (Fig. 7). The average cross phase estimate between ~2.4-myr
293 eccentricity AM and ~9 myr $\delta^{13}C$ cycles is about -180 degrees (Fig. 7). This supports the
294 antiphase relationship between eccentricity and $\delta^{13}C$ variations. However, visual examination
295 of the time series (Fig. 1, Cuves 3 and 4) indicates that $\delta^{13}C$ and eccentricity variations are
296 sometimes phase-shifted at the ~9 myr cyclicity suggesting that non-orbital processes (e.g.,
297 tectonics) could interfere into these long-term $\delta^{13}C$ oscillations (e.g., Zachos et al., 2001;
298 Leckie et al., 2002; Li et al., 2009). On the other hand, La2004 astronomical model (Laskar et
299 al., 2004) is valid for only the last 40 Ma, while the La2010d model (Laskar et al., 2011a) is
300 reliable for the last 50 Ma. Thus, correlation between $\delta^{13}C$ and astronomical variations for the
301 interval 50 to 67 Ma (Cb7 and Cb8) is critical, and should be considered with caution till a
302 future extended astronomical model will be available, and future studies could enhance
303 geological timescale resolution.
304
305 Besides, we note a positive correlation between $\delta^{13}C$ and astronomy for the last ~8
306 Ma. This exception may be due to the compilation of the carbon isotopes data itself, which
307 should be checked in future $\delta^{13}C$ compilations. In fact, possible unreliable $\delta^{13}C$ compiled data
308 could exist for the Plio-Pleistocene where basin to basin fractionation develops (low values of
309 the Pacific, J. Zachos, *pers. comm*). Recent studies concur with this hypothesis, and show
310 that Atlantic-Pacific $\delta^{13}C$ differential responses exist for the last ~10 Ma (Cramer et al., 2009,

311 their figure 6). A different hypothesis, Wang et al. (2010) suggested that the expression of
312 eccentricity in the $\delta^{13}C$ record is obscured for at least the last ~1.6 Ma, related to a major
313 change in the oceanic carbon reservoir associated with a restructuring of the Southern
314 Ocean. Finally, Katz et al. (2005) interpreted a long-term linear trend in this interval (precisely
315 for the last ~17 Ma, in their figure 1) as the result of a closing phase of the Wilson cycle,
316 when continents reassemble and the Atlantic Ocean basin closes. According to these
317 observations, we restrict our interpretation, in terms of possible orbital forcing of the 9-myr
318 $\delta^{13}C$ cycles, to the interval ~8 to ~50 Ma, and with caution the interval ~50 to ~60 Ma, where
319 9-myr $\delta^{13}C$ and eccentricity cycles are anticorrelated.
320
321 **5. Discussion: how does orbital forcing drive Cenozoic carbon cyclicity?**
322
323 High-amplitude (1‰) eccentricity-scale cyclicity has been described in various upper
324 Paleocene-Neogene $\delta^{13}C$ records (Woodruff and Savin, 1991; Flower and Kennett, 1995;
325 Diester-Haass, 1996; Zachos et al., 1996, 1997, 2001; Cramer et al., 2003; Pälike et al.,
326 2006a,b), suggesting that carbon recycling through the atmosphere-biosphere-ocean
327 reservoir (e.g., Siegenthaler and Sarmiento, 1993; Sarmiento and Bender, 1994)
328 preferentially responds to orbital eccentricity from modulation of the climatic precession. For
329 example, by applying climatic precession forcing to carbonate/organic carbon fluxes and
330 deposition, and the residence-time of carbon in the atmosphere-biosphere-ocean, Cramer et
331 al. (2003) modelled a theoretical eccentricity curve consistent with interpreted eccentricity
332 cycles (~100 and ~400 kyr) in their measured bulk carbonate $\delta^{13}C$. Specifically, they showed
333 a correspondence between maxima in ~400-kyr eccentricity and transient decreases in the
334 bulk carbonate $\delta^{13}C$ during the late Paleocene - early Eocene. In another example from the
335 Oligocene, Pälike et al. (2006a) demonstrated that long-term insolation forcing could
336 modulate atmospheric CO_2 levels as well as the oceanic carbonate ion (CO_3^{2-}) concentration,

337 leading to expansion and contraction of biospheric productivity in tune with long-term orbital
338 periodicities. Specifically, Pälike et al. (2006a) highlighted a strong ~400-kyr signal in the
339 $\delta^{13}C$ record, which they explained as the consequence of the long residence-time of carbon
340 in the oceans, leading to enhanced sensitivity to longer forcing periods.

341 In this study, we show a prominent ~9 myr cyclicity in $\delta^{13}C$ record, which may
342 correspond to ~9 myr AM cycles in orbital eccentricity variations. This is in accordance with
343 the idea of long residence-time of carbon in amplifying longer orbital periodicities. We also
344 note that the maxima of long-term $\delta^{13}C$ oscillations correspond to minima of long-term
345 eccentricity modulations (Figs. 1 and 2a), which again concurs with previous $\delta^{13}C$
346 cyclostratigraphic studies (Cramer et al., 2003; Pälike et al., 2006a, Rickaby et al., 2007; and
347 many others). Therefore, if there is a link between $\delta^{13}C$ record and orbital eccentricity
348 modulation at this multi-millionyear timescale, and considering previous studies in carbon-
349 cycle modeling, we could suggest that eccentricity induced insolation through its modulation
350 of the climatic precession may play an important role in carbon cycling, controlling a chain of
351 astro-climatically sensitive processes such as terrestrial weathering, biosphere productivity,
352 carbonate sedimentation and dissolution, burial and oxidation of organic carbon, etc (e.g.,
353 Westbroek et al., 1993; Cramer et al., 2003; Kurtz et al., 2003; Pälike et al., 2006a; Rickaby
354 et al., 2007; Li et al., 2009). At the same time, observed phase shifts between ~9-myr
355 eccentricity and $\delta^{13}C$ cycles suggest that additional processes (e.g., tectonics) could
356 contribute to the $\delta^{13}C$ variations.
357
358 Finally, the most prominent ~9-myr $\delta^{13}C$ cycle (Cb7, Figs. 1 and 2a), which
359 corresponds to a well expressed ~9-myr astronomical cycle in the eccentricity modulation,
360 includes the Paleocene-Eocene Thermal Maximum (PETM) event (Figs. 1 and 2b). In
361 particular, the PETM, which corresponds to a pronounced $\delta^{13}C$ negative excursion (2.5-3‰),
362 is situated within a strong decrease in the Cb7 $\delta^{13}C$ cycle, hinting at a possible link between

363 $\delta^{13}C$ rates and the occurrence of the event. The Cb7 cycle, especially its decreasing part,
364 seems to be amplified compared to the other ~9 myr $\delta^{13}C$ cycles (Fig. 1). This observation is
365 beyond the scope of our study, and needs, however, future work to model causes of rates in
366 the $\delta^{13}C$ variations and their link with the PETM onset in this specific interval of Cenozoic
367 (e.g., volcanism: Storey et al., 2007, and J. Zachos, pers. com; methane release from gas
368 hydrate: Dickens et al., 1995, 1997).
369
370
371 **6. Conclusions**
372
373 We show that Cenozoic carbon isotope record ($\delta^{13}C$) exhibits a multi-millionyear cycle
374 of a pseudo-periodicity close to 9 myr. Amplitude modulation (AM) analysis of astronomical
375 models shows that the ~2.4 myr eccentricity cycles are mainly modulated by ~9 myr cycles
376 similar to those observed in the $\delta^{13}C$ record. Several lines of correlation are observed
377 between ~9 myr eccentricity envelopes and $\delta^{13}C$ cycles pointing to a possible link between
378 the two.
379 Additionally, the Paleocene-Eocene Thermal Maximum (PETM) event, which
380 corresponds to a pronounced $\delta^{13}C$ negative excursion, coincides with a critical interval in the
381 ~9 myr $\delta^{13}C$ cycle. An unusual strong decrease in the most prominent ~9 myr $\delta^{13}C$ of the
382 Cenozoic may reflect specific processes in atmosphere-contient-ocean system (e.g.,
383 methane release from gas hydrate, volcanism), responsible for the amplification of the ~9
384 myr $\delta^{13}C$ cycle and the PETM excursion.
385
386
387 **Acknowledgments**
388

389 J. Laskar, B. Galbrun, and S. Boulila were supported by French ANR Grant ASTS-CM. J.
390 Laskar acknowledge the support from GENCI-CINES and PNP-CNRS. S. Boulila thanks
391 Linda Hinnov for help in time-series analysis and her revisions and comments on an earlier
392 version of the manuscript. We also thank Jim Zachos for help of the revised stable isotopes
393 data, and his comments and revisions on an earlier version of the manuscript. S. Boulila
394 thanks very much Jim Ogg (Purdue University) for help in geological timescale conversion.
395
396
397 **References**
398
399 Abels, H.A., Abdul Aziz, H., Krijgsman, W., Smeets, S.J.B., Hilgen, F.J., 2010. Long-period
400 eccentricity control on sedimentary sequences in the continental Madrid Basin (middle
401 Miocene, Spain). Earth Planet. Sci. Lett. 289, 220–231.
402 Archer, D., Maier-Reimer, E., 1994. Effect of deep-sea sedimentary calcite preservation on
403 atmospheric CO_2 concentration. Nature 367, 260–263.
404 Berger, A., Loutre, M.F., Laskar, J., 1992. Stability of the Astronomical Frequencies Over the
405 Earth's History for Paleoclimate Studies. Science 255, 560–566.
406 Billups, K., Pälike, H., Channell, J.E.T., Zachos, J.C., Shackleton, N.J., 2004. Astronomic
407 calibration of the late Oligocene through early Miocene geomagnetic polarity time scale.
408 Earth Planet. Sci. Lett. 224, 33–44.
409 Charles, A.J., Condon, D.J., Harding, I.C., Pälike, H., Marshall, J.E.A., Cui, Y., Kump, L.,
410 Croudace, I.W., in press. Constraints on the numerical age of the Paleocene/Eocene
411 boundary. http://www.agu.org/journals/pip/gc/2010GC003426-pip.pdf
412 Cramer, B.S., Wright, J.D., Kent, D.V., Aubry, M.P., 2003. Orbital climate forcing of $d^{13}C$
413 excursions in the late Paleocene-Eocene (Chrons C24n-C25n). Paleoceanography
414 18(4), 1097, doi: 10.1029/2003PA000909.

415 Cramer, B.S., Toggweiler, J.R., Wright, J.D., Katz, M.E., Miller, K.G., 2009. Ocean
416 overturning since the Late Cretaceous: Inferences from a new benthic foraminiferal
417 isotope compilation. Paleoceanography 24, PA4216, doi: 10.1029/2008PA001683.
418 Dickens, G.R., Castillo, M.M., Walker, J.C.G., 1997. A blast of gas in the latest Paleocene:
419 Simulating first order effects of massive dissociation of oceanic methane hydrate.
420 Geology 25, 259–262.
421 Dickens, G.R., O'Neil, J.R., Rea, D.K., Owen, R.M., 1995. Dissociation of oceanic methane
422 hydrate as a cause of the carbon isotope excursion at the end of the Paleocene.
423 Paleoceanography 10, 965–971.
424 Diester-Haass, L., 1996. Late Eocene-Oligocene paleoceanography in the southern Indian
425 Ocean (ODP Site 744). Mar. Geol. 130, 99–119.
426 Fienga, A., Manche, H., Laskar, J., Gastineau, M., 2008. INPOP06. A new numerical
427 planetary ephemeris. Astron. Astrophys. 477, 315–327.
428 Fienga, A., Laskar, J., Morley, T., Manche, H., Kuchynka, P., Le Poncin-Lafitte, C., Budnik,
429 F., Gastineau, M., Somenzi, L., 2009. INPOP08, a 4-D planetary ephemeris: from
430 asteroid and time-scale computations to ESA Mars Express and Venus Express
431 contributions. Astron. Astrophys. 507, 1675–1686.
432 Flower, B., Kennett, J., 1995. Middle Miocene deepwater paleoceanography in the southwest
433 Pacific: Relations with East Antarctic Ice Sheet development. Paleoceanography 10,
434 1095–1112.
435 Forte, A.M., Mitrovica, J.X., 1997. A resonance in Earth's obliquity and precession over the
436 past 20 Myr driven by mantle convection. Nature 390, 676–680.
437 Ghil, M., Allen, R.M., Dettinger, M.D., Ide, K., Kondrashov, D., Mann, M.E., Robertson, A.,
438 Saunders, A., Tian, Y., Varadi, F., Yiou, P., 2002. Advanced spectral methods for climatic
439 time series. Rev. Geophys. 40 (1), 3.1–3.41.
440 Gradstein, F.M., Ogg, J.G., Smith, A.G., 2004. A Geologic Time Scale 2004. Cambridge
441 University Press, 589 p.

442 Hays, J. D., Imbrie, J., Shackleton, N.J., 1976. Variations in the earth's orbit: pacemaker of
443 the ice ages. Science 194, 1121–1132.
444 Hilgen, F.J., Abdul Aziz, H., Krijgsman, W., Raffi, I., Turco, E., 2003. Integrated stratigraphy
445 and astronomical tuning of the Serravallian and lower Tortonian at Monte dei Corvi
446 (Middle-Upper Miocene, northern Italy). Palaeogeogr. Palaeoclimatol. Palaeoecol. 199,
447 229–264.
448 Hinnov, L.A., 2000. New perspectives on orbital stratigraphy. Ann. Rev. Earth Planet. Sci. 28,
449 419–475.
450 Huybers, P., Denton, G., 2008. Antarctic temperature at orbital time scales controlled by local
451 summer duration. Nature Geoscience 1, 787–792.
452 Imbrie, J., Hays, J.D., Martinson, D.G., McIntyre, A., Mix, A.C., Morley, J.J., Pisias, N.G.,
453 Prell, W.L., Shackleton, N.J., 1984. The orbital theory of Pleistocene climate: support
454 from a revised chronology of the marine $\delta^{18}O$ record. *In*: Berger A. *et al.* (eds.),
455 Milankovitch and climate. Understanding the response to astronomical forcing NATO.
456 *Advanced Science Institutes Series C.* 126, 269-305.
457 Katz, M.E., Wright, J.D., Miller, K.G., Cramer, B., Fennel, K., Falkowski, P.G., 2005.
458 Biological overprint of the global carbon cycle. Mar. Geol. 217, 323–338.
459 Kuiper, K.F., Deino, A., Hilgen, F.J., Krijgsman, W., Renne, P.R., Wijbrans, J.R., 2008.
460 Synchronizing Rock Clocks of Earth History. Science 320, 500-504.
461 Kurtz, A.C., Kump, L.R., Arthur, M.A., Zachos, J.C., Paytan, A., 2003. Early Cenozoic
462 decoupling of the global carbon and sulfur cycles. Paleoceanography 18, doi:
463 10.1029/2003PA000908.
464 Lagabrielle, Y., Goddéris, Y., Donnadieu, Y., Malavieille, J., Suarez, M., 2009. The tectonic
465 history of Drake Passage and its possible impacts on global climate. Earth Planet. Sci.
466 Lett. 279, 197–211.
467 Laskar J., 1990. The chaotic motion of the Solar System: A numerical estimate of the size of
468 the chaotic zone. Icarus 88, 266–291.

469 Laskar J., 1992. The limits of the Earth orbital calculations for geological time-scale use.
470 Royal Soc. (London), Phil. Trans. Ser. A 357, 1735–1759.
471 Laskar J., Fienga A., Gastineau M., Manche H., 2011a. La2010: A new orbital solution for the
472 long term motion of the Earth. Astron. Astrophys. 532, A89, doi: 10.1051/0004-
473 6361/201116836.
474 Laskar, J., Gastineau, M., Delisle, J.-B., Farrés, A., Fienga, A., 2011b. Strong chaos induced
475 by close encounters with Ceres and Vesta Astron. Astrophys., in press, manuscript no.
476 17504R.
477 Laskar J, Joutel F., Boudin F., 1993. Orbital, precessional, and insolation quantities for the
478 Earth from -20 Myr to + 10 Myr. Astron. Astrophys. 270, 522–533.
479 Laskar J., Robutel P., Joutel F., Gastineau M., Correia A. C. M., Levrard B., 2004. A long-
480 term numerical solution for the insolution quantities of the Earth. Astron. Astrophys. 428,
481 261–285.
482 Leckie, R.M., Bralower, T., Cashman, R., 2002. Oceanic anoxic events and plankton
483 evolution: Biotic response to tectonic forcing during the mid-Cretaceous.
484 Paleoceanography 17(3), doi: 10.1029/2001PA000623.
485 Li, G., Ji, J, Chen, J., Kemp, D.B., 2009. Evolution of the Cenozoic carbon cycle: The roles of
486 tectonics and CO2 fertilization. Glob. Biogeochem. Cycles 23, GB1009, doi:
487 10.1029/2008GB003220.
488 Lourens, L.J., Sluijs, A., Kroon, D., Zachos, J.C., Thomas, E., Röhl U., Bowles, J., Raffi, I.,
489 2005. Astronomical pacing of late Palaeocene to early Eocene global warming events.
490 Nature 435, 1083–108.
491 Mann, M.E., Lees, J.M., 1996. Robust estimation of background noise and signal detection
492 in climatic time series. Clim. Change 33, 409–445.
493 Mitchell, R.N., Bice, D.M., Montanari, A., Cleavel, L.C., Christianson, K.T., Coccioni, R.,
494 Hinnov, L.A., 2008. Oceanic Anoxic Cycles? Orbital prelude to the Bonarelli Level (OAE
495 2). Earth Planet. Sci. Lett. 267, 1–16.

496 Mitrovica, J.X., Forte, A.M., Pan, R., 1997. Glaciation-induced variations in the Earth's
497 precession frequency, obliquity and insolation over the last 2.6 Ma. Geophys. J. Intern.
498 128(2), 270–284.
499 Olsen, P.E., Kent, D.V., 1999. Long-term Milankovitch cycles from the Late Triassic and
500 Early Jurassic of eastern North America and their implications for the calibration of the
501 Early Mesozoic timescale and the long term behavior of the planets. Royal Soc.
502 (London), Phil. Trans. Ser. A. 357,1761–1788.
503 Paillard, D., Labeyrie, L., Yiou, P, 1996. Macintosch program performs timeseries analysis.
504 Eos 77, 379.
505 Pälike, H., Frazier, J., Zachos, J.C., 2006b. Extended orbitally forced palaeoclimatic records
506 from the equatorial Atlantic Ceara Rise. Quat. Sci. Rev. 25, 3138–3149.
507 Pälike, H., Laskar, J., Shackleton, N.J., 2004. Geologic constraints on the chaotic diffusion of
508 the Solar System. Geology 32, 929–932.
509 Pälike, H., Norris, R.D., Herrle, J.O., Wilson, P.A., Coxall, H.K., Lear, C.H., Shackleton, N.J.,
510 Tripati, A.K., Wade, B.S., 2006a. The Heartbeat of the Oligocene Climate System.
511 Science 314, 1894–1898.
512 Raymo, M.E., Ruddiman, W.F., 1992. Tectonic forcing of late Cenozoic climate. Nature 359,
513 117–122.
514 Rickaby, R.E.M., Bard, E., Sonzogni, C., Rostek, F., Beaufort, L., Braker, S., Rees, G.,
515 Schrag, D.P., 2007. Coccolith chemistry reveals secular variations in the global ocean
516 carbon cycle?. Earth Planet. Sci. Lett. 235, 83–95.
517 Sarmiento, J., Bender, M., 1994. Carbon biogeochemistry and climate change. Photosyn.
518 Res. 39, 209–234.
519 Shackleton, N.J., Crowhurst, S.J., Weedon, G.P., Laskar, J., 1999. Astronomical calibration
520 of Oligocene-Miocene time. Philos. Trans. R. Soc. London A 357, 1907–1929.
521 Siegenthaler, U., Sarmiento, J., 1993. Atmospheric carbon dioxide and the ocean. Nature
522 365, 119–125.

523 Standish, E.M., 1998. JPL Planetary and Lunar Ephemerides, DE405/LE405. Jet Propulsion
524 Laboratory, Interoffice Memorandum, IOM 312.F – 98 – 048.
525 Storey, M., Duncan, R.A., Ill, C.C., 2007. Paleocene-Eocene Thermal Maximum and the
526 Opening of the Northeast Atlantic. Science 316, 587–589.
527 Thomson, D.J., 1982. Spectrum estimation and harmonic analysis. IEEE Proc. 70, 1055–
528 1096.
529 van Dam, J.A., Abdul, Aziz, H., Sierra, M.A.A., Hilgen, F.J., van den Hoek Ostende, L.W.,
530 Lourens, L.J., Mein, P., van der Meulen, A.J., and Pelaez-Campomanes, P., 2006. Long-
531 period astronomical forcing of mammal turnover. Nature 443, 687–691.
532 Wade, B.S., Pälike, H., 2004. Oligocene climate dynamics. Paleoceanography 19, PA4019,
533 doi: 10.1029/2004PA001042.
534 Westbroek, P., Brown, C.W., Vanbleijswijk, J., Brownlee, C., Brummer, G.J., Conte, M.,
535 Egge, J., Fernandez, E., Jordan, R., Knappertsbusch, M., Stefels, J., Veldhuis, M.,
536 Vanderwal, P., Young, J., 1993. A model system approach to biological climate forcing:
537 the example of *Emiliania huxleyi*. Glob. Planet. Change 8, 27–46.
538 Westerhold, T., Röhl, U., Laskar, J., Raffi, I., Bowles, J., Lourens, L.J., Zachos, J.C., 2007.
539 On the duration of Magnetochrons C24r and C25n, and the timing of early Eocene global
540 warming events: Implications from the ODP Leg 208 Walvis Ridge depth transect.
541 Paleoceanography 22(PA2201): doi:10.1029/2006PA001322.
542 Westerhold, T., Röhl, U., McCarren, H.K., Zachos, J.C., 2009. Latest on the absolute age of
543 the Paleocene – Eocene Thermal Maximum (PETM): new insights from exact
544 stratigraphic position of key ash layers +19 and -17. Earth Planet. Sci. Lett. 287, 412–
545 419.
546 Westerhold, T., Röhl, U., Raffi, I., Fornaciari, E., Monechi, S., Reale, V., Bowles, J., Evans,
547 H.F., 2008. Astronomical calibration of the Paleocene time. Palaeogeogr.
548 Palaeoclimatol. Palaeoecol. 257, 377–403.

549 Woodruff, F., Savin, S., 1991. Mid-Miocene isotope stratigraphy in the deep sea: High-
550 resolution correlations, paleoclimatic cycles, and sediment preservation.
551 Paleoceanography 6, 755–806.
552 Zachos, J.C., Dickens, G.R., Zeebe R.E., 2008. An early Cenozoic perspective on
553 greenhouse warming and carbon-cycle dynamics. Nature 451, 279–283.
554 Zachos, J.C., Flower, B., Paul, H., 1997. Orbitally paced climate oscillations across the
555 Oligocene/Miocene boundary. Nature 388, 567–570.
556 Zachos, J.C., Pagani, M., Sloan, L., Thomas, E., Billups, K., 2001. Trends, Rhythms,
557 Aberrations in Global Climate 65 Ma to Present. Science 292, 686–693.
558 Zachos, J.C., Quinn, T., Salamy, K., 1996. High-resolution (10^4 years) deep-sea foraminiferal
559 stable isotope records of the Eocene-Oligocene climate transition. Paleoceanography
560 11, 251–266.
561
562

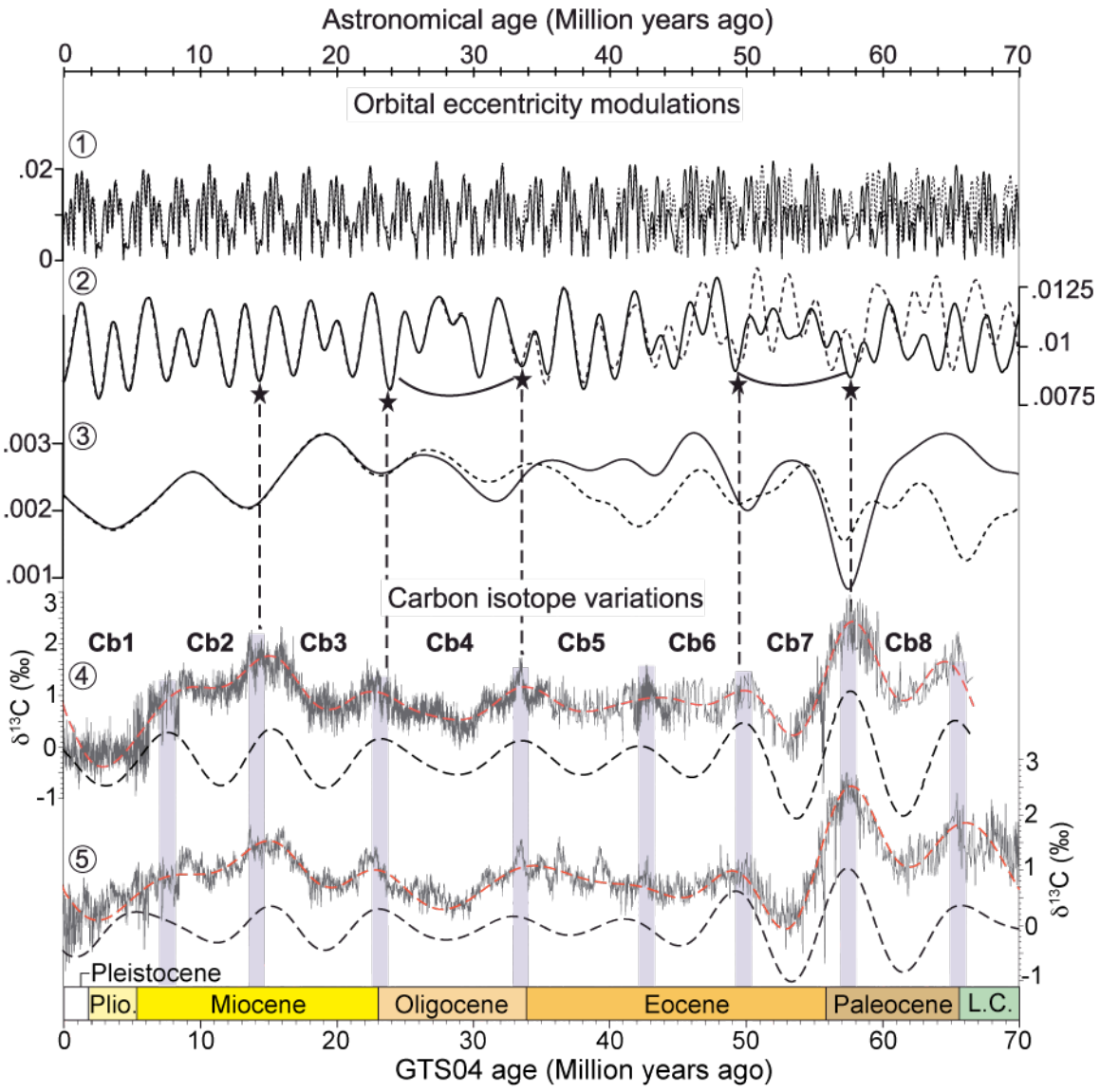

Figure 1: Amplitude modulations (AM) of the nominal La2004 (solid curves) and La2010d (dashed cuves) astronomical models (Laskar et al., 2004, and Laskar et al., 2011a), and correlation with the ~9 myr $\delta^{13}C$ cyclicity of deep-sea $\delta^{13}C$ records (Zachos et al., 2001, 2008; Cramer et al., 2009). Top to bottom, **curve 1**: AM of the short eccentricity band (9.4 ±2 myr^{-1}), **curve 2** : inverted AM of the ~400-kyr eccentricity band (2.5 ±0.5 myr^{-1}), **curve 3**: AM of the ~2.4-myr eccentricity band (0.4245 ± 0.1350 myr^{-1}). **curves 4** : raw $\delta^{13}C$ record (Zachos et al., 2001, 2008), also shown low-pass (0 to 0.17 myr^{-1} band) and bandpass (0.1265 ±0.04245 myr^{-1}) filtered $\delta^{13}C$ record, the ~9-myr $\delta^{13}C$ oscillations are shown (labelled Cb1 to Cb8 delimited by vertical bars), **curves 5**: $\delta^{13}C$ record (Cramer et al., 2009) with 5 point running average. Low-pass (0 to 0.17 myr^{-1} band) and bandpass

(0.1265 ±0.04245 myr^{-1}) filtered δ^{13}C record is also shown, applied to the raw δ^{13}C data (resampled to 0.004 myr). For filtering, we used a Gaussian filter (Paillard et al., 1996). All filtering in orbital eccentricity was carried out on the -10 to 75 Ma interval to avoid filter-edge effect. AM analysis was performed by Hilbert transformation (e.g., p. 435 in Hinnov, 2000). The vertical dashed lines represent the correlation between the 'Cb' cycles and the astronomical ~9-myr cycles, with emphasis on five tie-points (represented with black stars) which show good correlation of Cb3, Cb4, and Cb7 to their equivalent astronomical cycles (vertical dashed lines: possible bundling of four ~2.4 myr cycles).

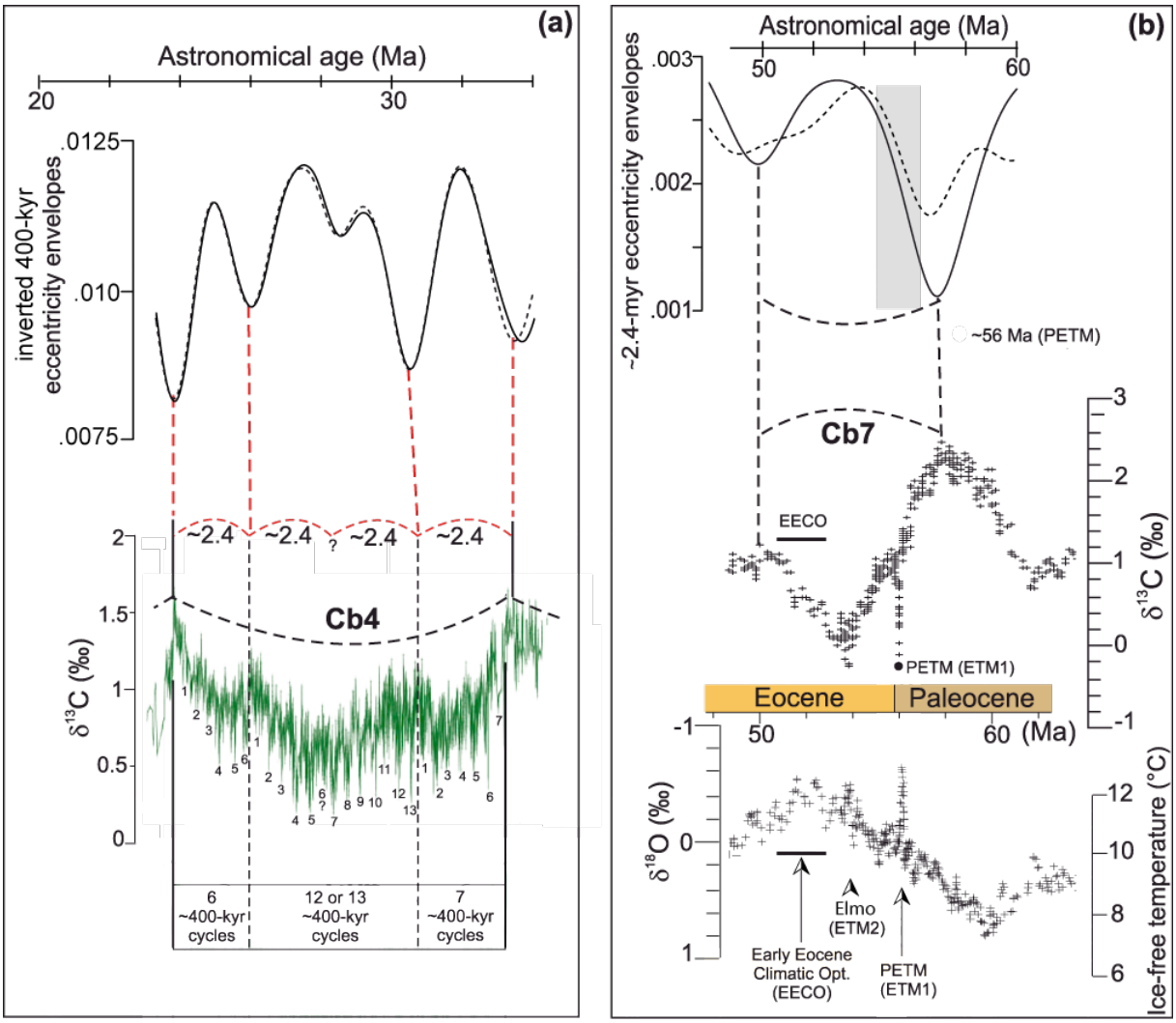

Figure 2: Details of ~9-myr cycles show a good correlation between δ^{13}C record and AM eccentricity, and the position of δ^{13}C brief events (δ^{18}O is also shown, from

586 Supplementary Figure S1). **(a)** The Cb4 $\delta^{13}C$ cycle correlates to the ~9-myr astronomical
587 cycle (from Fig. 1, curve 2). The two middle ~2.4-myr cycles are “amalgamated” in both
588 the $\delta^{13}C$ and the astronomical signal. This supports the validity of the astronomical
589 models. **(b)** The Cb7 $\delta^{13}C$ cycle correlates to the ~9-myr astronomical cycle (from Fig. 1,
590 curve 3), but should be considered with caution given that neither the geological time
591 scale nor the astronomical models are precise in this time interval. The vertical bar
592 indicates the interval (~54.5 to ~56.2 Ma) including the PETM event (56 Ma, estimates
593 are from Westerhold et al., 2007, 2008, 2009, and Kuiper et al., 2008; 55.9 Ma according
594 to Charles et al., in press). Both the PETM and the Elmo (ETM2) events are situated in
595 the decreasing part of the strongest ~9-myr $\delta^{13}C$ cycle (Cb7) with the PETM is near the
596 inflection-point (~56 Ma).
597

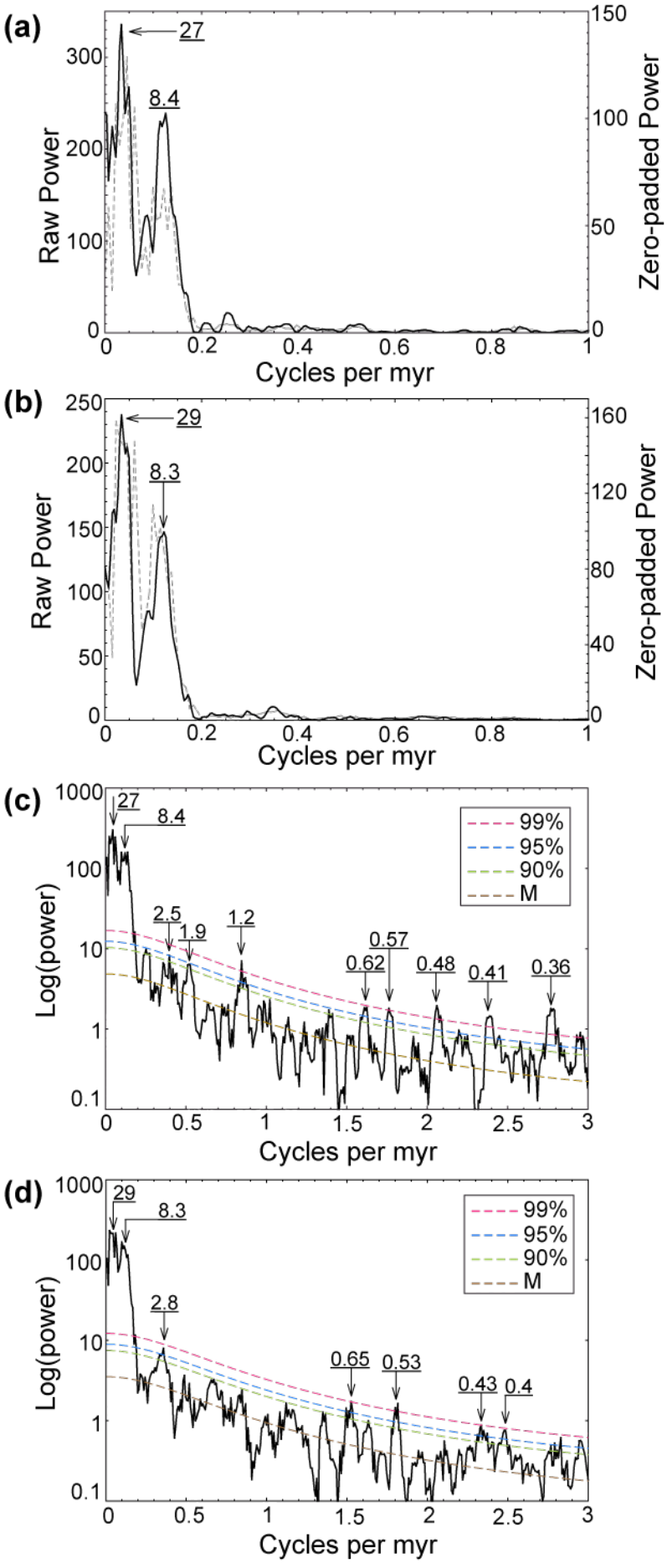
(a)
27
8.4
Raw Power
Zero-padded Power
Cycles per myr
(b)
29
8.3
Raw Power
Zero-padded Power
Cycles per myr
(c)
27
8.4
2.5
1.9
1.2
0.57
0.62
0.48
0.41
0.36
99%
95%
90%
M
Log(power)
Cycles per myr
(d)
29
8.3
2.8
0.65
0.53
0.43
0.4
99%
95%
90%
M
Log(power)
Cycles per myr

598

599 **Figure 3:** 2π-MTM power spectra of the $\delta^{13}C$ records (Zachos et al., 2008; Cramer et al.,
600 2009), using the multitaper method (Thomson, 1982) as implemented in SSA-MTM
601 Toolkit (Ghil et al., 2002). Results of noise modelling (also shown) were estimated using
602 linear fitting and median filtering over 20% of the average Nyquist frequency range. **(a)**
603 Zachos et al.'s (2008) compilation, dashed line: raw $\delta^{13}C$ record linearly interpolated to a
604 ~4-kyr sample rate **(**the average sampling interval of the record is ~4.7 kyr), solid line: 1x
605 zero-padded $\delta^{13}C$ used to highlight the ~8.4-myr peak (see also Fig. S2). **(b)** Cramer et
606 al.'s (2009) compilation, dashed line: raw $\delta^{13}C$ record linearly interpolated to a ~4-kyr
607 sample rate **(**the average sampling interval of the record is ~4.7 kyr), solid line: 1x zero-
608 padded $\delta^{13}C$ used to highlight the ~8.3-myr peak (see also Fig. S2). **(c)** Spectrum of (a)
609 in a logarithmic format over a broader frequency band, together with the modeled red
610 noise spectrum. **(d**) Spectrum of (b) in a logarithmic format over a broader frequency
611 band, together with the modeled red noise spectrum.
612

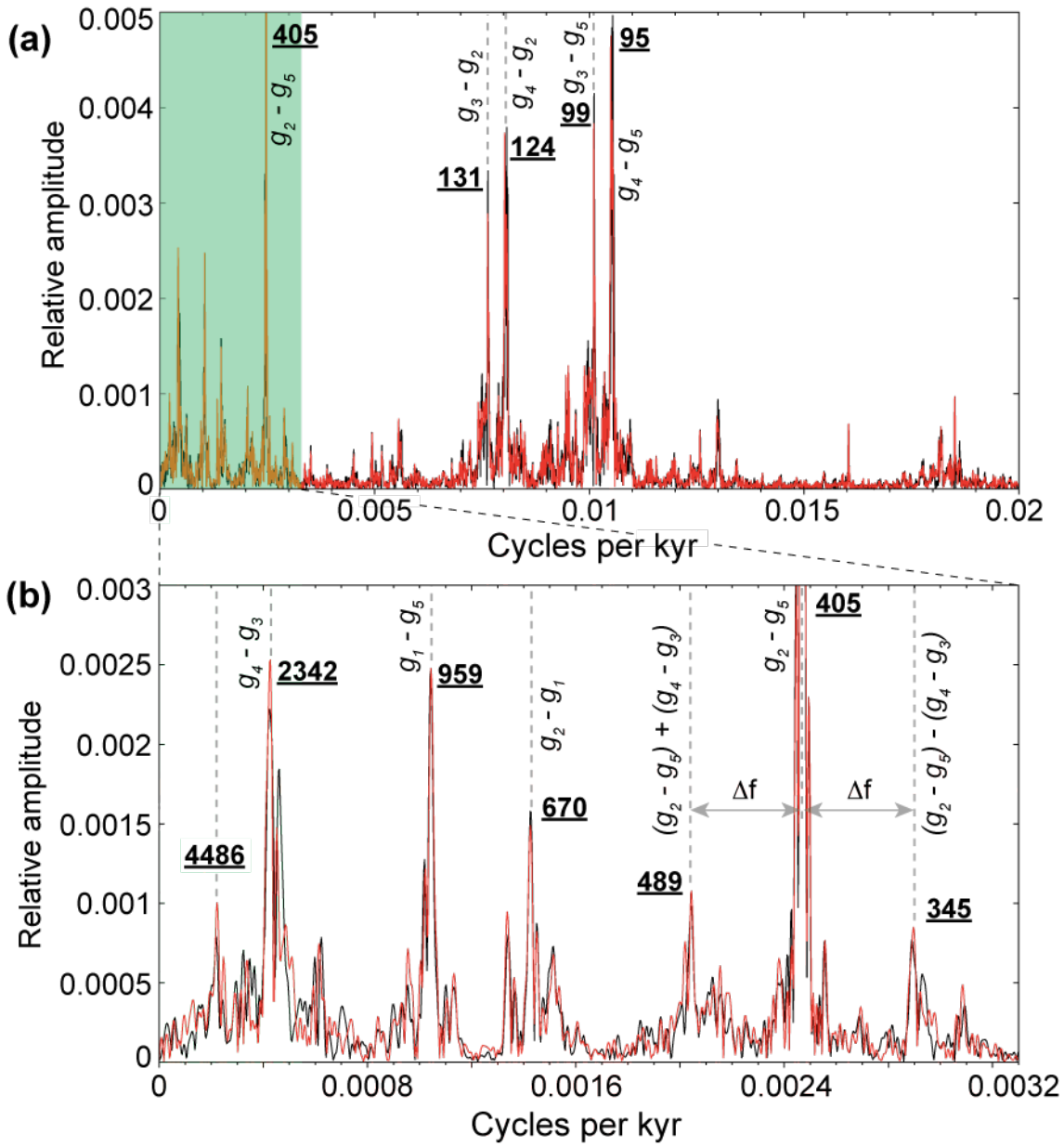

Figure 4: 2π-MTM harmonic analysis of the orbital eccentricity in the La2004 (black line) and La2010d (red line) astronomical models (Laskar et al., 2004, 2011a) over the last 67 Ma (time interval equivalent to that in $\delta^{13}C$ data). **(a)** the raw spectra displayed over frequencies 0 to 0.02 cycles/kyr, and truncated amplitude axis at 0.005: only the peak representing the 405 kyr eccentricity term is truncated (its full relative amplitude is ~0.010). He truncated power axis to highlight peaks at low frequencies in the shaded area. **(b)** a zoom of the shaded area in 'a' to well visualize low-frequency peaks, the amplitude axis is also truncated at 0.003. All peaks are labelled in kyr, and the origin of each eccentricity component is also shown, where g1, g2, g3, g4 and g5 are the secular

frequencies related respectively to the precession of the perihelions of Mercury, Venus, the Earth, Mars, and Jupiter (see Laskar et al., 2004 for detail). Note that only the main peaks depicting the main eccentricity components are shown. Δf in 'b' equals to 0.000427 cycles/kyr, which corresponds to a period of 2342 kyr, i.e., (g4 – g3) is the result of two possible interferences of (g2 – g5) with (g2 – g5) – (g4 – g3), and (g2 – g5) with (g2 – g5) + (g4 – g3) (see text for discussion).

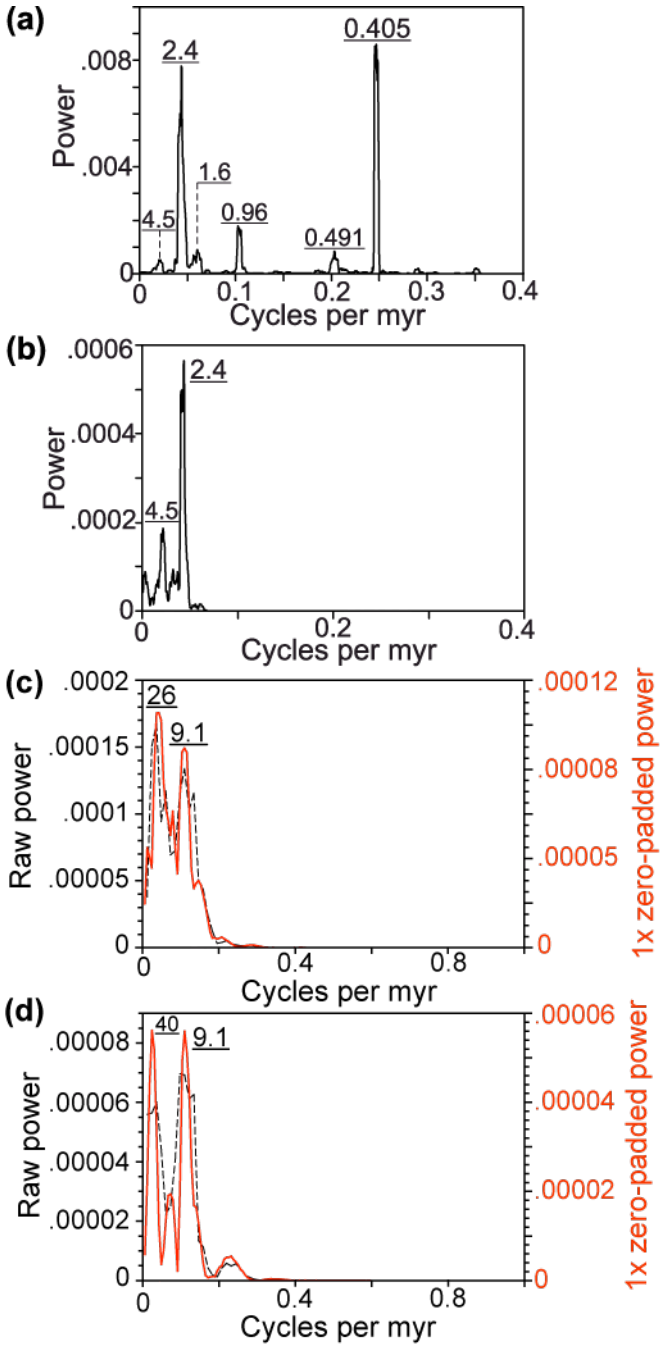

631 **Figure 5:** 2π-MTM power spectra of amplitude modulation (AM) of $\delta^{13}C$ records (Zachos et
632 al., 2008; Cramer et al., 2009), using the multitaper method (Thomson, 1982) as
633 implemented in SSA-MTM Toolkit (Ghil et al., 2002). Results of noise modelling (also
634 shown) were estimated using linear fitting and median filtering over 20% of the average
635 Nyquist frequency range. **(a)** Spectrum of the AM envelopes of the ~400-kyr $\delta^{13}C$ band
636 of Zachos et al.'s (2008) compilation (Supplementary Figure S3, solid curve 5). **(b)**
637 Spectrum of the AM envelopes of the ~400-kyr $\delta^{13}C$ band of Cramer et al.'s (2009)
638 compilation (Supplementary Figure S3, dashed curve 5). **(c)** Spectrum of the AM
639 envelopes of the ~2.4-myr $\delta^{13}C$ band of Zachos et al.'s (2008) compilation
640 (Supplementary Figure S3, solid curve 4), dashed line: raw AM, solid line: 1x zero-
641 padded AM. **(d)** Spectrum of the AM envelopes of the ~2.4-myr $\delta^{13}C$ band of Cramer et
642 al.'s (2009) compilation (Supplementary Figure S3, solid curve 4), dashed line: raw AM,
643 solid line: 1x zero-padded AM. All peaks are labelled in myr.
644

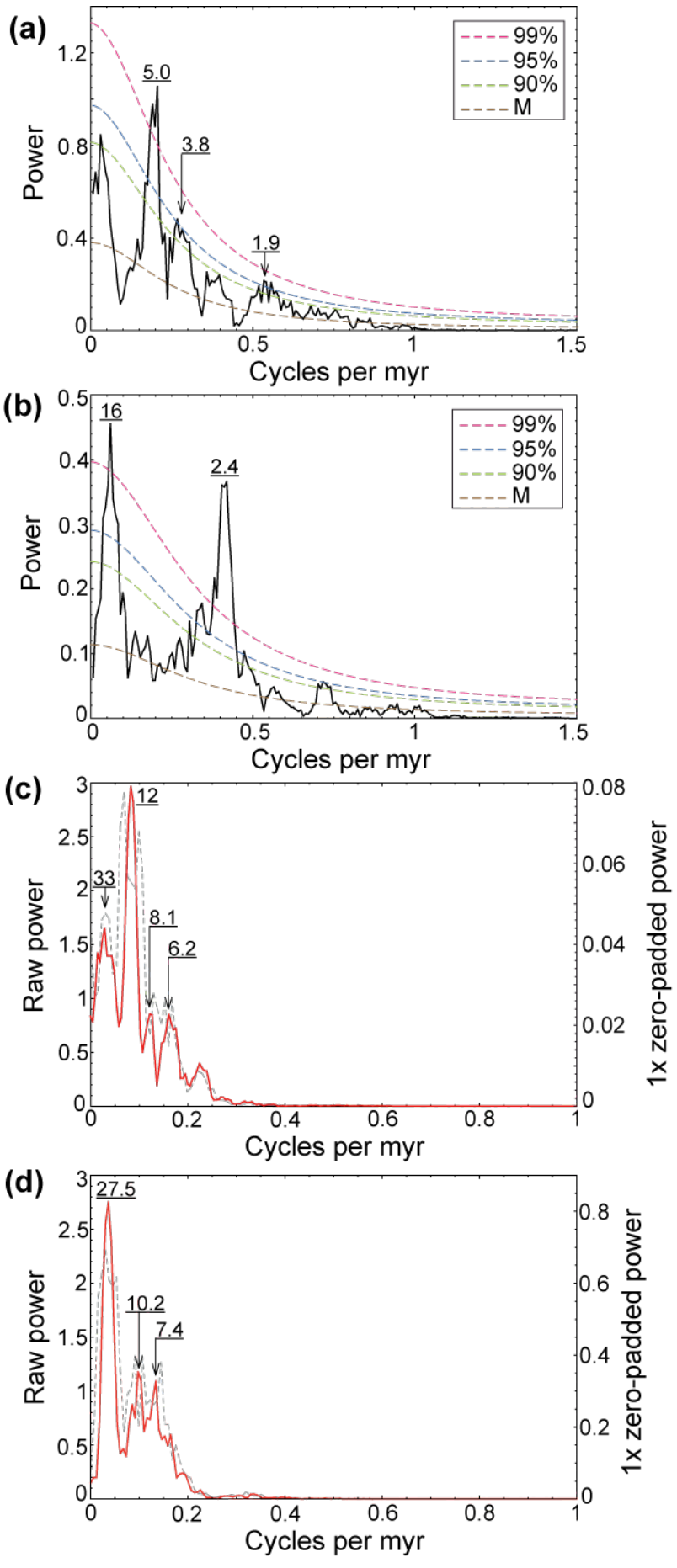
(a)
99%
95%
90%
M
5.0
3.8
1.9
Power
Cycles per myr
(b)
16
2.4
Power
Cycles per myr
(c)
12
33
8.1
6.2
Raw power
1x zero-padded power
Cycles per myr
(d)
27.5
10.2
7.4
Raw power
1x zero-padded power
Cycles per myr

645

Figure 6: 2π-MTM power spectra of amplitude modulations (AM) of La2004 and La2010d orbital eccentricity (Laskar et al., 2004, 2011a), using the multitaper method (Thomson, 1982) as implemented in SSA-MTM Toolkit (Ghil et al., 2002). **(a)** AM of the ~100-kyr La2004 eccentricity band (Fig. 1, solid curve 1). **(b)** AM of the ~400-kyr La2004 eccentricity band (Fig. 1, solid curve 2). **(c)** Dashed line: AM of the ~2.4-myr La2004 eccentricity band (Fig. 1, solid curve 3), solid line: 1x zero-padded of ~2.4-myr La2004 eccentricity AM used to highlight the ~9-myr peak. **(d)** Dashed line: AM of the ~2.4-myr La2010d eccentricity band (Fig. 1, dashed curve 3), solid line: 1x zero-padded of ~2.4-myr La2010d eccentricity AM used to highlight the ~9-myr peak. All peaks are labelled in myr.

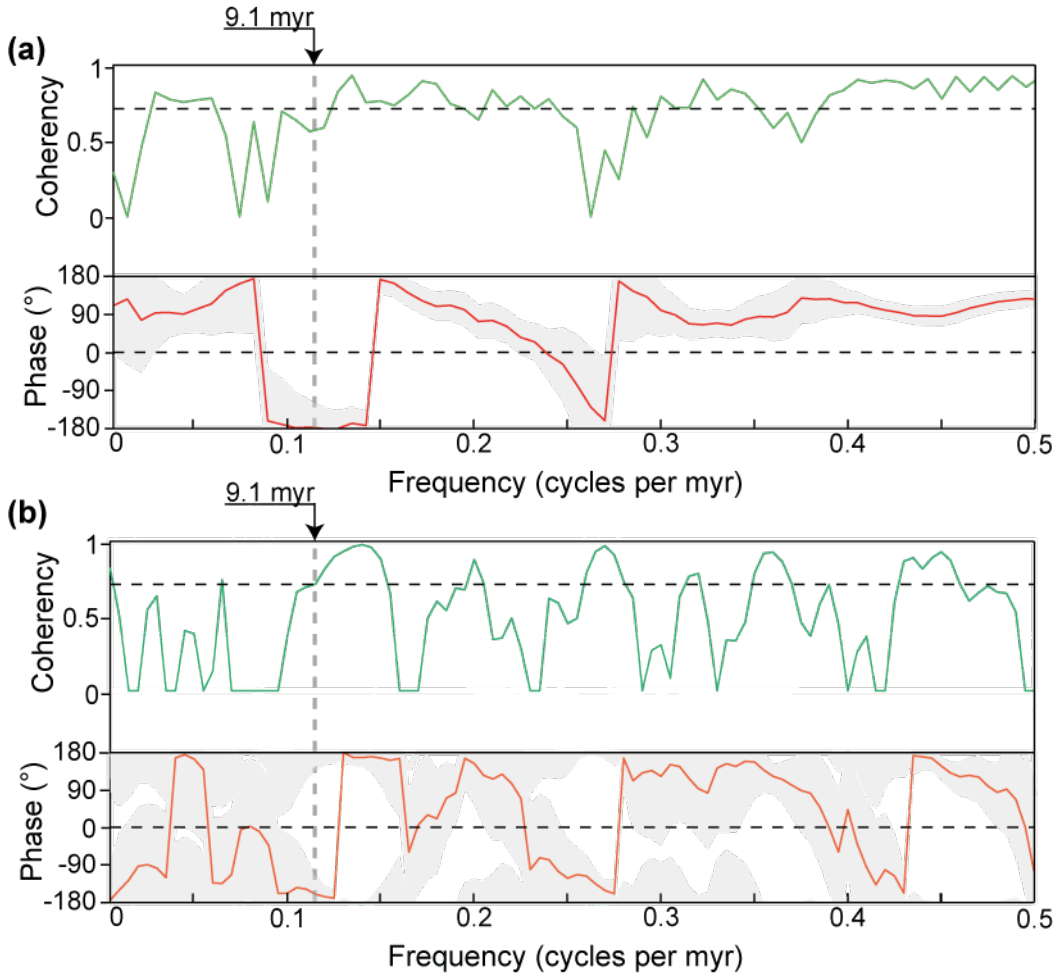

Figure 7: Coherency and cross-phase spectral analysis of envelopes of ~2.4 myr cycles of

659 eccentricity time series (Fig. 1, Curve 3) versus ~9 myr $\delta^{13}C$ cycles (from the raw $\delta^{13}C$
660 record of Zachos et al., 2008 in Fig. 1, Curve 4). **(a)** $\delta^{13}C$ versus ~2.4 myr AM of La2004
661 model (Laskar et al., 2004). **(b)** $\delta^{13}C$ versus ~2.4 myr AM of La2010d model (Laskar et
662 al., 2011a). Note that $\delta^{13}C$ and eccentricity are coherent at ~9 myr cyclicity, and that ~9
663 myr $\delta^{13}C$ oscillations are ~180° out of phase with ~9 myr eccentricity cycles. The
664 approximate 95% confidence level for the coherence between red noise and a narrow
665 band signal is indicated by the dashed line; the zero phase line is indicated by the
666 dashed line, and the approximate 95% confidence interval for phase is indicated by the
667 gray shading. Vertical dashed lines indicate the ~9.1 myr frequency (see Figs. 5c,d). We
668 used the cross-MTM method in the Matlab routine of Peter Huybers (e.g., Huybers and
669 Denton, 2008).
670
671
672
673 **Boulila et al.'s Supplementary Information**
674
675 **Supplementary figures**
676

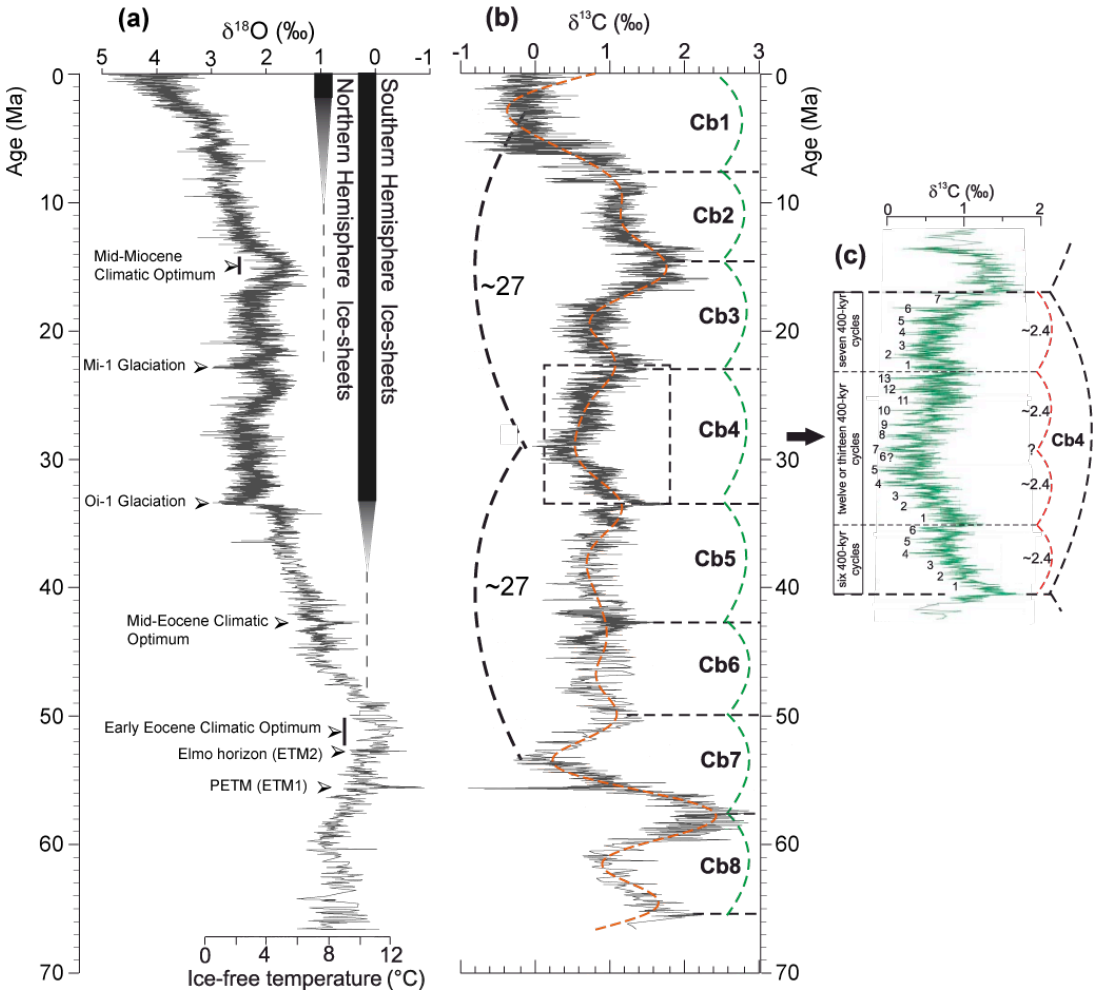

677

678 **Figure S1:** Global deep-sea oxygen and carbon isotope records based on data compiled
679 from more than 40 Deep Sea Drilling Project and Ocean Drilling Program sites (Zachos
680 et al., 2001, 2008). **(a)** Oxygen record, the main climatic events are also shown, ETM1
681 (also known as the Elmo horizon) and ETM2 (also known as PETM) represent Eocene
682 Thermal Maximum events, with the PETM is the Paleocene-Eocene Thermal Maximum,
683 the main hyperthermal event. Note that the $\delta^{18}O$ temperature scale was computed for an
684 ice-free ocean (~1.2 ‰ standard mean ocean water, SMOW). From the early Oligocene
685 on, and possibly for some time before that, much of the variability in the $\delta^{18}O$ values may
686 reflect volume changes in polar ice sheets. The vertical bars provide a rough estimate of
687 the ice volume in each hemisphere relative to the ice volume during the Last Glacial
688 Maximum. **(b)** Carbon isotope record, pseudo-periodic ~9-myr (~7 to ~11 myr) $\delta^{13}C$
689 cycles are shown (labelled Cb1 to Cb8). Possible ~27-myr $\delta^{13}C$ cycles are also shown.

690 **(c)** A detailed Cb4 cycle, data from Pälike et al. (2006a) with ~4-kyr sampling intervals.
691 We identified the ~400-kyr and ~2.4-myr cycles within Cb4. The two middle ~2.4-myr
692 cycles are "amalgamated", as are the analogous astronomical ~2.4-myr cycles over this
693 time interval (see Figs. 1 and 2a).
694

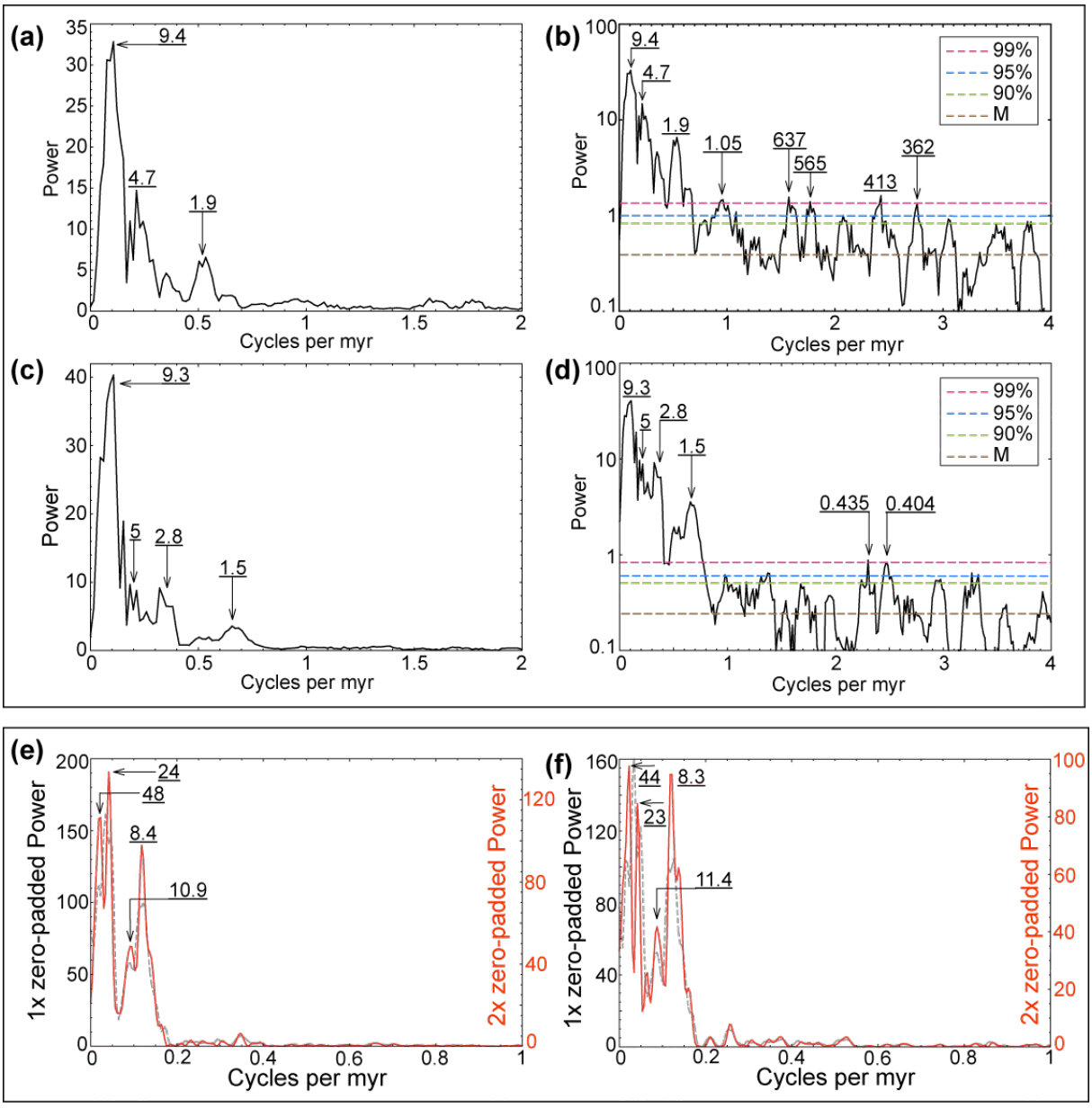

695

696 **Figure S2: Upper panel**: 2π-MTM power spectra of a selected interval (16.5 to 54.5 Ma) of
697 Cenozoic $\delta^{13}C$ records, after removal of a third-order polynomial fit to attenuate irregular
698 long-term variations due to the ~27- and 29-myr oscillations (spectral peaks in main Fig.
699 3a,b). **(a)** Spectrum in a linear scale of the $\delta^{13}C$ of Zachos et al.'s (2001, 2008)

compilation. **(b)** Spectrum of 'a' in a logarithmic scale over a broader frequency band, together with the modeled robust red noise spectrum. **(c)** Spectrum in a linear scale of the $\delta^{13}C$ of Cramer et al.'s (2009) compilation. **(d)** Spectrum of 'c' in a logarithmic scale over a broader frequency band, together with the modeled robust red noise spectrum. Results of noise modelling: Curve M is the linear median-smoothed, fitted robust red noise spectrum; the upper 90%, 95% and 99% confidence limits. Note that the srongest spectral peak is centred on ~9 myr period in both compilations (Zachos et al., 2001, 2008, and Cramer et al., 2009). This supports the prominence and robustness of the 9 myr $\delta^{13}C$ oscillations (see text for discussion). **Lower panel:** 2π-MTM power spectra of Cenozoic $\delta^{13}C$ records of Zachos et al.'s (2008) compilation **(a)** and Cramer et al.'s (2009) compilation **(b)**. Spectra of 1x zero-padded time series (grey-dashed line as in main Figs. 3a,b) and spectra of 2x zero-padded time series (red solid line). Note that the 2x zero-padding enhances the resolution of the ~8.5 and ~25 myr peaks. The ~46 myr (48 myr in 'e' and 44 myr in 'f') peak may represent a single oscillation delimited by Cb2/Cb3 and Cb7/Cb8 boundaries (Fig. S1). We used the multitaper method (Thomson, 1982) as implemented in SSA-MTM Toolkit (Ghil et al., 2002). All peaks are labelled in myr.

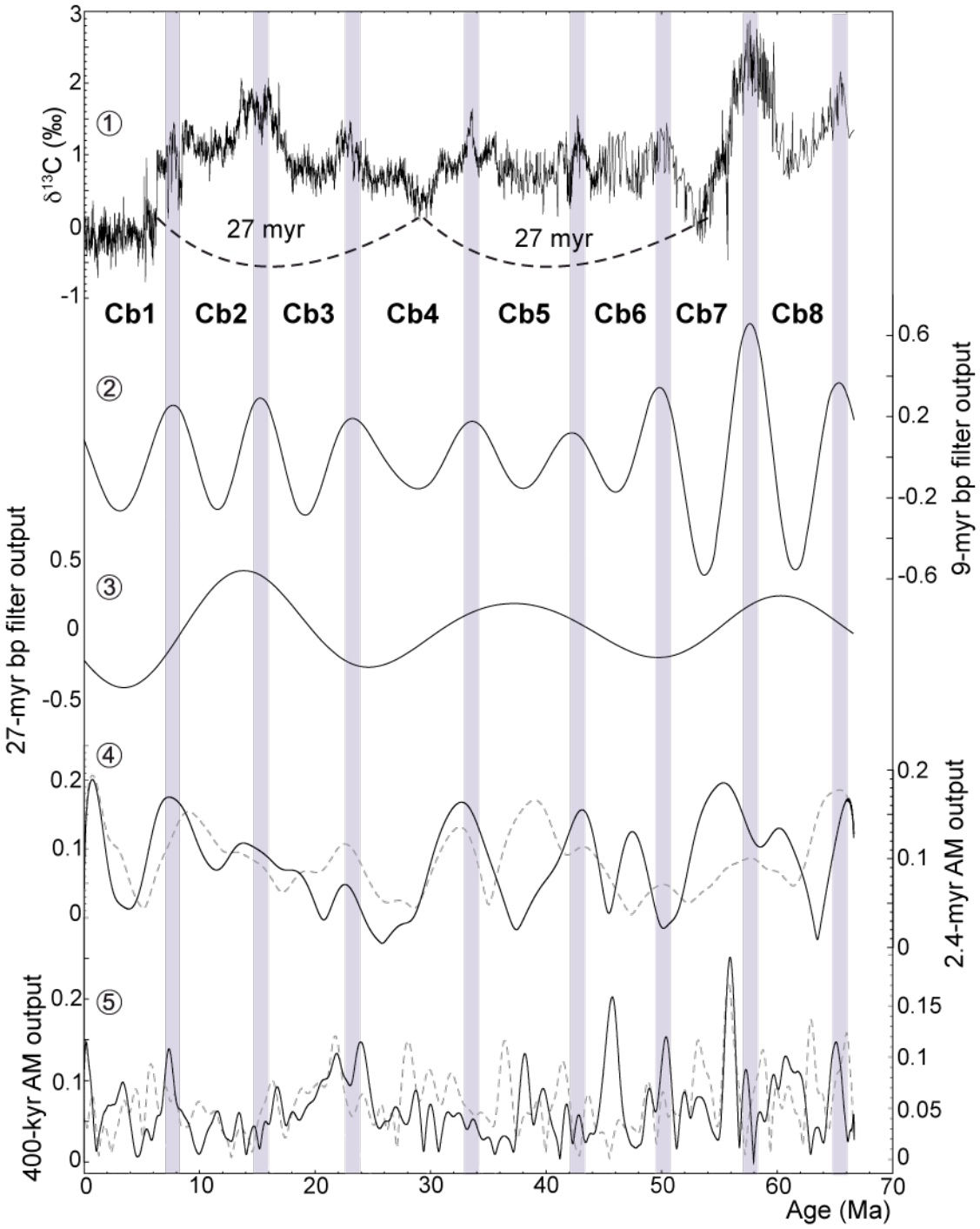

Figure S3: Amplitude modulations (AM) time series of the raw $\delta^{13}C$ records (Zachos et al., 2001, 2008, Cramer et al., 2009). From top to bottom: **curve 1**: $\delta^{13}C$ record of Zachos et al. (2008) with 5-point running average, the ~9-myr $\delta^{13}C$ pseudo-periodic oscillations (labelled Cb1 to Cb8) and the possible ~27-myr cycles are shown, **curve 2**: ~9-myr bandpass filter output of Zachos et al.'s (2008) raw $\delta^{13}C$ (0.1265 ±0.0435 myr^{-1} band), **curve 3**: ~25-myr bandpass filter output of Zachos et al.'s (2008) raw $\delta^{13}C$ (0.048 ±0.015

myr^{-1} band), **curve 4**: AM envelopes of the ~2.4-myr eccentricity band (0.4245 ± 0.1350 myr^{-1} band), solid black curve: AM applied to Zachos et al.'s (2008) raw δ^{13}C, dashed-grey curve: AM applied to Cramer et al.'s (2009) raw δ^{13}C, **curve 5**: AM envelopes of the ~400-kyr eccentricity band (2.5 ±0.5 myr^{-1} band), solid black curve: AM applied to Zachos et al.'s (2008) raw δ^{13}C, dashed-grey curve: AM applied to Cramer et al.'s (2009) raw δ^{13}C. All band-pass filtering was performed using a Gaussian filter (Paillard et al., 1996). Before analysis, δ^{13}C data are resampled and linearly interpolated each 0.004 myr for both compilations.

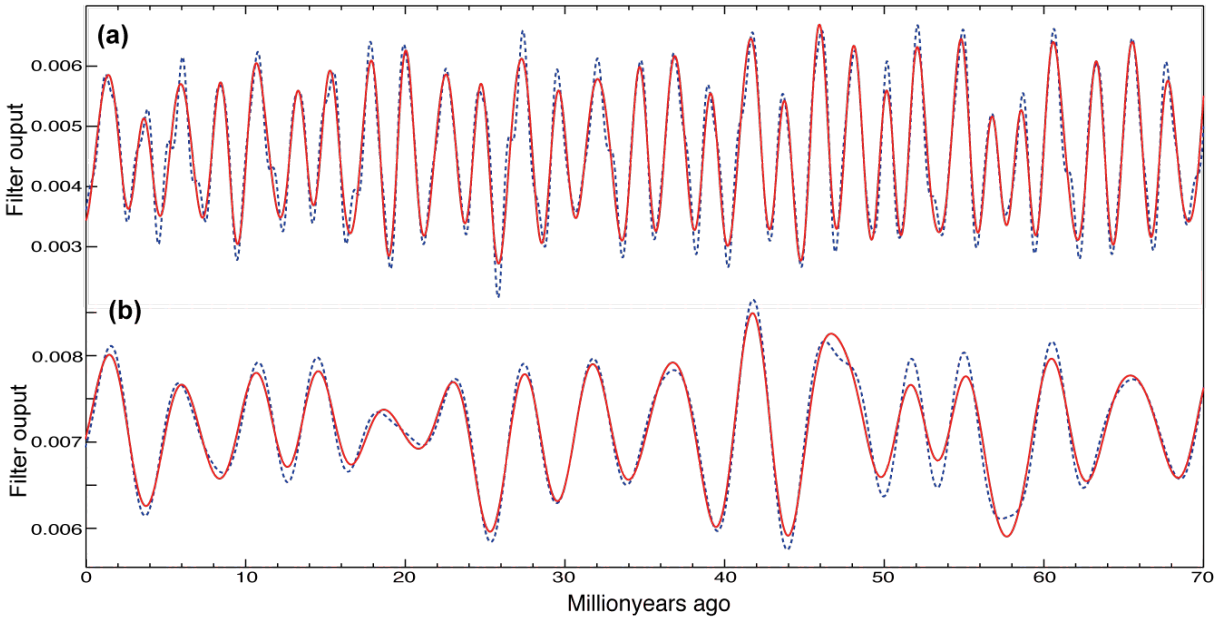

Figure S4: Low-pass filtering of the La2004 raw eccentricity time series (Laskar et al., 2004) to extract the resonant cyclicities corresponding to the argument $\theta = 2(g_4 - g_3) - (s_4 - s_3)$ (Laskar, 1990; Laskar et al., 1992), where g_3, g_4 are related to the precession of the perihelions of the Earth and Mars, s_3, s_4 are related to the precession of the nodes of the same planets. **(a)** ~2.4 myr eccentricity cycles extracted with two different frequency-cutoff bands, a moderate band (0 to 0.7 cycles/myr, solid line) and a large band (0 to 0.5 cycles/myr, dashed line). **(b)** ~4.5 myr eccentricity cycles extracted with two different

744 frequency-cutoff bands, a moderate band (0 to 0.28 cycles/myr, solid line) and a large
745 band (0 to 0.33 cycles/myr, dashed line). All low-pass filtering was performed using the
746 Taner filter (Taner, 2000).